

Supernova Progenitors, Their Variability, and the Type IIP Supernova ASASSN-16fq in M 66

C. S. Kochanek^{1,2}, M. Fraser³, S. M. Adams⁴, T. Sukhbold^{1,2}, J. L. Prieto^{5,6},
T. Müller^{6,7}, G. Bock⁸, J. S. Brown¹, Subo Dong⁹, T. W.-S. Holoien¹, R. Khan¹⁰,
B. J. Shappee^{11,12}, K. Z. Stanek^{1,2}

¹ Department of Astronomy, The Ohio State University, 140 West 18th Avenue, Columbus OH 43210

² Center for Cosmology and AstroParticle Physics, The Ohio State University, 191 W. Woodruff Avenue, Columbus OH 43210

³ Institute of Astronomy, University of Cambridge, Madingley Rd, Cambridge CB3 0HA, UK

⁴ Cahill Center for Astrophysics, California Institute of Technology, Pasadena, CA 91125, USA

⁵ Núcleo de Astronomía de la Facultad de Ingeniería, Universidad Diego Portales, Av. Ejército 441, Santiago, Chile

⁶ Millennium Institute of Astrophysics, Santiago, Chile

⁷ Instituto de Astrofísica, Pontificia Universidad Católica de Chile, Av. Vicuña Mackenna 4860, 782-0436 Macul, Santiago, Chile

⁸ Runaway Bay Observatory, Australia

⁹ Kavli Institute for Astronomy and Astrophysics, Peking University, Yi He Yuan Road 5, Hai Dian District, Beijing 100871, China

¹⁰ Department of Astronomy, Box 351580, University of Washington, Seattle, WA 98195

¹¹ Carnegie Observatories, 813 Santa Barbara Street, Pasadena, CA 91101, USA

¹² Hubble, Carnegie-Princeton Fellow

2 September 2016

ABSTRACT

We identify a pre-explosion counterpart to the nearby Type IIP supernova ASASSN-16fq (SN 2016cok) in archival Hubble Space Telescope (HST) data. The source appears to be a blend of several stars that prevents obtaining accurate photometry. However, with reasonable assumptions about the stellar temperature and extinction, the progenitor almost certainly had an initial mass $M_* \lesssim 17M_\odot$ and was most likely in the mass range $M_* = 8\text{--}12M_\odot$. Observations once ASASSN-16fq has faded will have no difficulty accurately determining the properties of the progenitor. In 8 years of Large Binocular Telescope (LBT) data, no significant progenitor variability is detected to RMS limits of roughly 0.03 mag. Of the six nearby SN with constraints on low level variability, SN 1987A, SN 1993J, SN 2008cn, SN 2011dh, SN 2013ej and ASASSN-16fq, only the slowly fading progenitor of SN 2011dh showed clear evidence of variability. Excluding SN 1987A, the 90% confidence limit implied by these sources on the number of outbursts over the last decade before the SN that last longer than 0.1 years (FWHM) and are brighter than $M_R < -8$ mag is approximately $N_{out} \lesssim 3$. Our continuing LBT monitoring program will steadily improve constraints on pre-SN progenitor variability at amplitudes far lower than achievable by SN surveys.

Key words: stars: massive – supernovae: general – supernovae: individual: SN 2016cok – galaxies: individual: NGC 3627

1 INTRODUCTION

At the end of their lives, all massive ($\gtrsim 8M_\odot$) stars must undergo core collapse once their iron cores become too massive to be stable. In most cases, this leads to a supernova (SN) explosion probably driven by some combination of neutrino heating and the effects of turbulence and convection (see the recent review by Müller (2016) and, e.g., recent results by Couch & Ott 2015, Dolence et al. 2015, Wongwathanarat et al. 2015). The visible properties of the

successful SNe then depend on the degree of mass loss, ranging from Type IIP SN which have retained most of their hydrogen envelopes, to Type Ic SN which appear to have been stripped even of helium (e.g., Filippenko 1997). The mass loss is controlled by some combination of intrinsic effects such as winds and extrinsic effects such as binary mass transfer (see the review by Smith 2014).

There is no strong requirement that more than roughly 50% of core collapses lead to successful SN (e.g., neutrino backgrounds, Lien et al. 2010; star formation rates,

Horiuchi et al. 2011; nucleosynthesis, Brown & Woosley 2013, Clausen et al. 2015) and a 10-30% fraction of failed SN producing black holes without a dramatic external explosion is both expected in many modern analyses of the “explodability” of stars (e.g., Ugliano et al. 2012, O’Connor & Ott 2013, Pejcha & Thompson 2015, Ertl et al. 2016, Sukhbold et al. 2016) and would provide a natural explanation of the compact remnant mass function (Kochanek 2014, Kochanek 2015, Clausen et al. 2015). Indeed, scenarios for the recent gravitational wave detection of a merging black hole binary (Abbott et al. 2016) all invoke at least one failed SN (e.g., Belczynski et al. 2016, Woosley 2016).

A powerful means of probing these issues is to work out the mapping between successful SNe and their progenitor stars. This is a challenging observational program (see the reviews by Smartt 2009 and Smartt 2015) which has slowly been carried out over the last 20 years (e.g., Van Dyk et al. 2003, Smartt et al. 2004, Li et al. 2006, Smartt et al. 2009, Elias-Rosa et al. 2009, Elias-Rosa et al. 2011, Maund et al. 2011, Van Dyk et al. 2011, Fraser et al. 2012, Fraser et al. 2014). With one possible exception (Cao et al. 2013, Folatelli et al. 2016, see Eldridge et al. (2013) for a discussion of limits), all the identified progenitors are of Type II (IIP, IIL, IIb, or IIn).

As first pointed out by Kochanek et al. (2008) and then better quantified by Smartt et al. (2009), there appears to be a deficit of higher mass SN progenitors. In particular, Smartt et al. (2009) only identified Type IIP progenitors with masses of $\lesssim 17M_{\odot}$ even though stars up to $25\text{--}30M_{\odot}$ are expected to explode as red supergiants with most of their hydrogen envelopes. While attempts have been made to explain this using extinction by winds (Walmswell & Eldridge 2012, but see Kochanek et al. 2012a) or by modifying stellar evolution (e.g. Groh et al. 2013), the same problem of missing, higher mass progenitors is seen in examinations of the stellar populations near local group SN remnants (Jennings et al. 2014). Jerkstrand et al. (2014) also argue that no Type IIP SN have shown nucleosynthetic evidence for a higher mass ($M_{*} > 20M_{\odot}$) progenitor. Following the proposal of Kochanek et al. (2008), Gerke et al. (2015) have been carrying out a search for failed SN with the Large Binocular Telescope (LBT), identifying one promising candidate (see also Reynolds et al. 2015). The progenitor of this candidate for a failed SN appears to be a red supergiant in exactly the mass range missing from searches for the progenitors of successful SN (Adams et al. 2016, in preparation).

A second recent puzzle about SN progenitors is that some appear to have outbursts (Pastorello et al. 2007, Fraser et al. 2013, Mauerhan et al. 2013, Ofek et al. 2014, Ofek et al. 2016) and/or eject significant amounts of mass (see Gal-Yam 2012, Smith 2014) shortly before they explode. The most extreme mass-loss events ($\dot{M} \sim M_{\odot}/\text{year}$) likely explain the rare, superluminous Type IIn SNe (Smith & McCray 2007), but the inferred mass loss rates are frequently $\dot{M} \gtrsim 10^{-3}M_{\odot}/\text{year}$ even for normal Type IIn SNe (see, e.g., Kiewe et al. 2012). The local systems known to reach such extreme mass loss rates are the Luminous Blue Variables (LBVs), with η Carinae as the most spectacular example (see Humphreys & Davidson 1994). The rate of η Carinae-like events is roughly 10% of the SN rate (Kochanek 2011, Khan et al. 2015a, Khan et al. 2015b),

which is sufficient to explain the occurrence of the extreme Type IIn superluminous SN. Any association of LBV eruptions with the very late phases of stellar evolution would roughly require the typical $M_{*} \gtrsim 50M_{\odot}$ star to have at least one eruption in the $\sim 10^3$ year period after carbon ignition (Kochanek 2011). On the other hand, theoretical models to explain pre-SN outbursts and Type IIn SNe have favored mechanisms associated with the last few years, corresponding to the neon/oxygen burning phases or later (Quataert & Shiode 2012, Shiode & Quataert 2014, Smith & Arnett 2014, Woosley & Heger 2015). In this picture, massive stars must have two separate mechanisms for triggering outbursts, one to explain the LBVs and a second to explain the pre-SN outbursts.

The existence of any transients associated with the last $\lesssim 10^3$ years (or less) of stellar life requires a causal mechanism associated with these final phases (see the discussion in Kochanek 2011). Figure 1 shows the dependence of the final nuclear burning stages on progenitor mass for the standard, non-rotating, $12\text{--}100M_{\odot}$, solar metallicity models of Sukhbold & Woosley (2014) and Woosley & Heger (2007). We show the periods of core and shell carbon, oxygen and silicon burning – the neon burning phase is not as energetically important. The large scale structure in Figure 1, with the shortest time scales for intermediate masses, is driven by the rapid increase in mass loss for the higher mass stars. The smaller scale variations in the mass-dependence of the post-carbon burning phases are due to the complex interplay of the burning phases and their consequences for structure of the stellar core (see Sukhbold & Woosley (2014) for a detailed discussion).

We illustrate the outbursts associated with Type IIn SN in Figure 1 by SN 2009ip and the Palomar Transient Factory (PTF) sample of Type IIn SN considered by Ofek et al. (2014). SN 2009ip has an estimated progenitor mass of $50\text{--}80M_{\odot}$ (Smith et al. 2010) and showed a series of outbursts before the apparent explosion (see, e.g., Smith et al. 2010, Foley et al. 2011, Mauerhan et al. 2013, Pastorello et al. 2013, Margutti et al. 2014). For the PTF sample, the progenitor masses are unknown. PTF data are available for the last few years before the SN, as shown by the lines spanning the survey times for each SN. Ofek et al. (2014) detect 5 outbursts and argue that it is highly probable that all Type IIn SN experience outbursts and that many are simply missed due to the survey depth and cadence. The outbursts shown in Figure 1 are associated with the very last phases of carbon shell burning through the early phases of oxygen shell burning. It seems probable, particularly in the case of SN 2009ip, that outbursts cannot be restricted to the time period after the initiation of core oxygen burning. As a contrast, if the eruption mechanism of LBVs had any correlation with these last phases, it would have to be associated with the carbon burning phase, as illustrated in Figure 1 by the 1840 and 1655 outbursts of η Car and P Cygni (see Humphreys & Davidson 1994).

Broadly speaking, there are two possible scenarios associated with these pre-SN transients. The first option is that only the high amplitude events seen in the SN surveys or implied by the Type IIn SNe exist and they are associated with a very narrow range of progenitor parameter space (e.g. mass, metallicity, rotation). The second option is that the outburst mechanism is relatively generic, and the existing

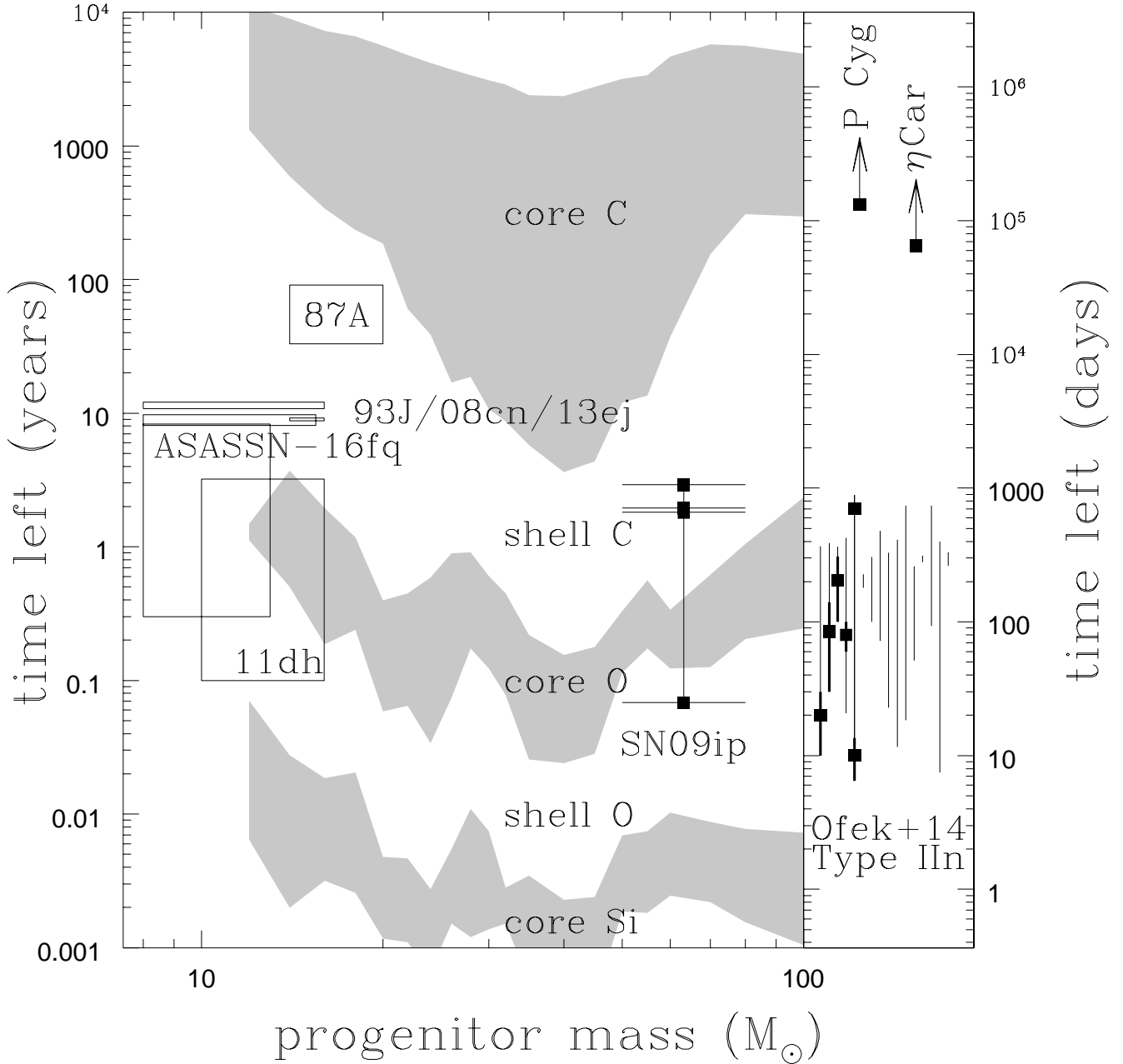


Figure 1. Final nuclear burning stages as a function of progenitor mass based on the standard, non-rotating, 12–100 M_{\odot} , solar metallicity models of Sukhbold & Woosley (2014) and Woosley & Heger (2007). The gray bands show, from top to bottom, the periods of core carbon, oxygen and silicon burning, separated by periods of shell burning. The points associated with SN 2009ip indicate the timing of its outbursts relative to its presumed explosion along with its estimated mass range. The sub-panel to the right shows 16 thin vertical lines for the (control) time periods sampled by PTF for 16 Type IIn SN, with heavy black points and lines for the time periods associated with outbursts (Ofek et al. 2014). The masses of the progenitors of these stars are unknown but they are generally assumed to be large. For comparison, the sub-panel also indicates the present day lower limits for the 1840 and 1655 outbursts of η Car and P Cyg. The boxes at lower masses show the progenitor mass ranges and the time periods that can be surveyed for progenitor variability for SN 1987A, SN 1993J, SN 2008cn, SN 2011dh, SN 2013ej, and ASASSN-16fq. For a Salpeter IMF with SN occurring in the mass range from 8 to 100 M_{\odot} , 50% of SN arise from the mass range from 8 to 13.1 M_{\odot} .

events simply represent the high amplitude tail of a much broader distribution. Unfortunately, the existing systematic searches for outbursts (e.g. Ofek et al. 2014, Bilinski et al. 2015, Strotjohann et al. 2015) are all part of searches for supernovae and essentially cannot detect significantly lower amplitude transients.

Like building the mapping between SN and progenitors, building the mapping between pre-SN outbursts and progenitors requires surveys of much greater sensitivity than searches for SN. Unfortunately, where data deep enough to observe progenitors are already rare, having multiple epochs of such data to study progenitor variability is rarer still. At present, such data only exists for the progenitors of SN 1987A (see Plotkin & Clayton (2004) and references therein), SN 1993J (Cohen et al. 1995), SN 2008cn (Elias-Rosa et al. 2009, Maund et al. 2015), SN 2011dh (Szczygiel et al. 2012), and SN 2013ej (Fraser et al. 2014). These sources all have progenitor detections and mass estimates, placing them below $20M_{\odot}$. Figure 1 shows the region of progenitor mass and remaining life time the data can probe. The variability constraints for SN 1987A and SN 1993J are relatively poor and only SN 2011dh shows clear evidence for low levels of variability. All these systems are also in the $\lesssim 20M_{\odot}$ mass range suggested by Shiode & Quataert (2014) for wave-driven mass loss at solar metallicity and some are likely near the $\sim 10M_{\odot}$ mass range associated with the explosive silicon burning mechanism of Woosley & Heger (2015).

Here we report on the properties of the progenitor of ASASSN-16fq (SN 2016cok). ASASSN-16fq was discovered (Bock et al. 2016) in NGC 3627 (M 66) by the All-Sky Automated Survey for Supernovae (ASAS-SN, Shappee et al. 2014) on 28 May 2016 and was spectroscopically classified as a Type IIP SN (Zhang et al. 2016). There are multiple epochs of HST data because of the debated transient SN 1997bs (Van Dyk et al. 2000, Smith et al. 2011, Kochanek et al. 2012b, Adams & Kochanek 2015) and the Type IIL SN 2009hd (Elias-Rosa et al. 2011, Tinyanont et al. 2016). It is also one of the galaxies monitored as part of the search for failed supernovae with the LBT (Kochanek et al. 2008, Gerke et al. 2015), allowing a deep search for progenitor variability over its last 8 years (see Figure 1). In §2 we identify and describe the progenitor primarily based on archival HST data to make a rough estimate of its luminosity and initial mass. In §3, we search for variability from the progenitor using the data from the LBT. We discuss the results in §4, focusing on an extended discussion of supernova progenitor variability. Following Gerke et al. (2015), we adopt a distance of 10.62 Mpc from Kanbur et al. (2003) and a Galactic extinction of $E(B - V) = 0.03$ mag from Schlafly & Finkbeiner (2011).

2 IDENTIFICATION AND PROPERTIES OF THE PROGENITOR

The region including ASASSN-16fq was observed by HST on 28 December 1994 (WFPC2/F606W, GO-54456, PI Illingworth), 26 November 2001 (WFPC2/F606W, GO-8597, PI Regan), 24 February and 4 March 2001 (WFPC2/F555W and F814W, GO-8602, PI Filippenko), 30/31 December 2004 (ACS/F658N and F435W, GO-10402, PI Chandar),

14 December 2009 (ACS/F555W and F814W, GO-11575, PI Van Dyk), and 28 November 2013 (WFC3/UVIS/F555W and F814W, GO-13477, PI Kochanek). These data are summarized in Table 1. The region has also been observed multiple times by Spitzer at 3.6 and $4.5\mu\text{m}$ (programs 159, 10001 and 10136/11063, PIs Kennicutt, Kochanek and Kasliwal, respectively).

In order to determine the position of the SN in the HST images, we obtained new LBT data including the SN consisting of 24 five second R-band exposures with a $1''.05$ full width at half-maximum (FWHM) and a nominal R-band depth when combined of roughly 24.7 mag ($S/N \simeq 5$). We identified 39 sources in common between the combined LBT image and the pipeline, drizzled, CTE-corrected (charge transfer efficiency) ACS/WFC F814W HST image taken on 2009 December 14. A pixel coordinate transformation allowing for rotation, translation, independent x and y pixel scalings and second order x^2 , xy and y^2 terms to account for distortions (24 coefficients in total) led to a geometric transformation with root-mean-square (RMS) errors in the x and y HST pixel axes of 0.164 and 0.169 LBT pixels, respectively. The position of the SN in the LBT image was measured using three different centering algorithms which agreed to $\lesssim 0.02$ LBT pixels (pixel scale $0''.226$). The resulting estimate of the pixel position of the SN on the F814W image is $(1658.047 \pm 0.734, 2014.933 \pm 0.757)$. Figure 2 shows the LBT image with the SN and the same region in the pre-explosion HST image along with an inset showing a $3''.0$ -square region centered on the estimated position of the progenitor. A source is readily apparent at this position.

The pixel coordinates of this pre-explosion source are measured to be $(1657.612 \pm 0.094, 2014.856 \pm 0.048)$ using the average results of three different centering algorithms in IRAF PHOT. This is offset from our estimated position of the SN by $(0.435, 0.077)$ ACS pixels, or $0''.022$ in total. Thus, the SN and our progenitor candidate have formally coincident positions given their respective uncertainties. However, this source also appears to be an extended blend of several stars, with a FWHM of 3 pixels instead of the ~ 2 pixels found for nearby point sources. This proves to be a considerable complication for our photometric measurements.

For photometry, we used HSTPHOT for the WFPC2 images and DOLPHOT for the ACS and WFC3 images (Dolphin 2000). HSTPHOT is designed specifically for point-spread function (PSF)-fitting photometry on WFPC2 images, while DOLPHOT is a more general version of HSTPHOT which can also handle ACS and WFC3 data. ACS, WFC3 and WFPC2 all have different pixel scales, and the observations summarized in Table 1 were taken with a range of orientations and depths. Hence, it is difficult to directly compare observations taken with each of these cameras particularly when the decomposition of the blended sources is not unique. The photometric results are reported in Table 1 along with any magnitudes for the source available from the Hubble Source Catalog (HSC, Whitmore et al. 2016) for comparison. All the reported magnitudes are in the Vega system, with appropriate transformations from the AB magnitudes used by the HSC.

The WFPC2 images were obtained with the WF3 detector, which has a pixel scale of $0''.1$ that grossly under samples the PSF. The 1994 images were very shallow and there was a slight (~ 2 pix) offset between the two exposures, so we ran

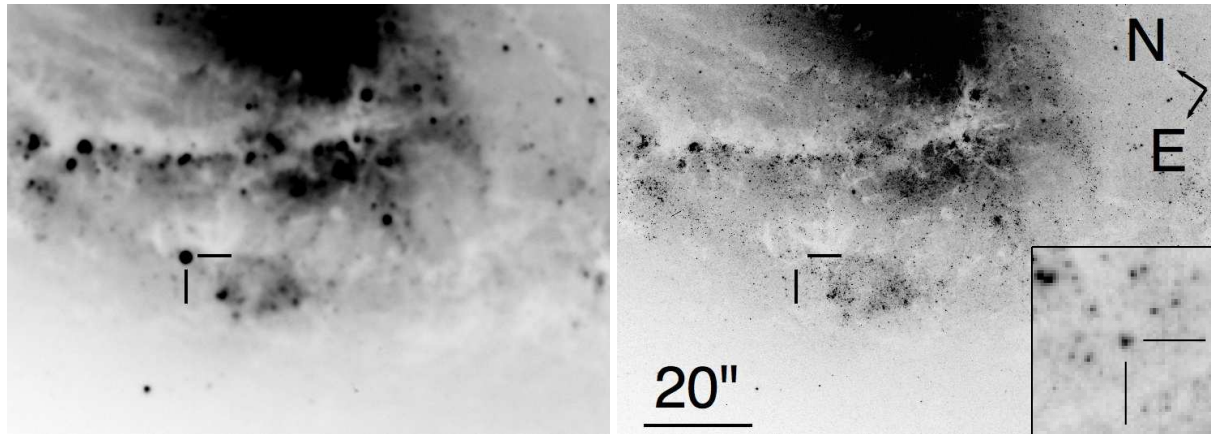


Figure 2. Identification of a progenitor candidate for ASASSN-16fq. The left panel shows an image of the SN taken with LBT, aligned to the pre-explosion HST ACS/WFC F814W image shown in the right panel. The position of the SN is indicated in both panels. The inset in the right, pre-explosion panel shows a $3'0 \times 3'0$ region centered on the progenitor candidate, with the derived SN position indicated.

HSTPHOT on each frame individually. For the WFPC2 data from 2001, there was no dithering between the exposures, so we combined the two images available for each filter. Cosmic rays were rejected using the paired exposures for each pointing. HSTPHOT was run using its recommended parameters, performing PSF-fitting photometry with a detection threshold of 3.5σ , and simultaneously refitting the sky background (option 512). Aperture corrections were derived from the data, and applied to the measured magnitudes along with standard CTE corrections.

In all of the WFPC2 images, the progenitor candidate was detected as a single source, as shown in Fig. 3. The 1994 and 2001 F606W magnitudes differ by almost 0.5 mag despite using identical settings for HSTPHOT. If we take 5 nearby sources with F606W ~ 22 mag, we find that the sources all appear to be brighter in 2001 by 0.15 to 0.35 mag. The cause of the discrepancy is unclear, although the 1994 exposures were significantly shallower and have lower backgrounds that would worsen the effects of CTE. We applied the HOTPANTS difference imaging package to the two F606W epochs and found no significant residuals, indicating that there was no significant variability associated with the source. We will not consider the 1994 data further. The HSC had an estimate for the source flux in the 2001 F814W image, and the HST magnitude was consistent with our photometry to <0.1 mag.

The ACS images were analyzed with DOLPHOT. The drizzled ACS reference image (file type `_drc`) for each filter was used to identify sources, while photometric measurements were performed on the individual, undrizzled, `_flc` files. Both file types are corrected for CTE losses, so no CTE corrections were applied to the measured magnitudes. The pipeline-reduced 2004 ACS `_flc` files did not have a cosmic ray mask in their data quality extension. We processed these files with ASTRODRIZZLE to derive a cosmic ray mask before carrying out the remainder of the analysis. The DOLPHOT parameters, including the choice of aperture radius, were matched to those of the ANGST survey (Dalcanton et al. 2009). We used a large 8 pixel aperture, fitting each source, its neighbors and the background simultaneously. We used a 3σ source detection threshold and set the `force=1` param-

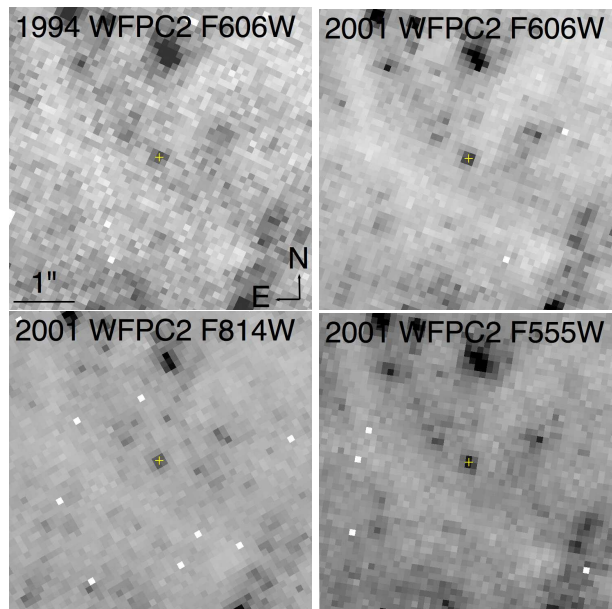


Figure 3. WFPC2 images ($5'0$ square, North up) from 2001 centered on the candidate progenitor. The progenitor candidate is marked by the yellow cross. The white squares are bad pixels.

eter to force all objects to be fit as point sources. For the F658N image, DOLPHOT failed to detect enough sources to align the two `_flt` images to the drizzled `F658N` reference image. Here we measured the positions of many point-like sources common to each image within IRAF, and used ACS-FITDISTORT within DOLPHOT to align the frames. The location of the SN in each of the images was found by aligning them to the 2009 F814W image which was used to identify the progenitor.

DOLPHOT splits the flux from the source at the progenitor position into a number of sources, which is not surprising given that that its FWHM is broader than other nearby, point-like sources. If we disable the `force=1` option, the source is modeled as a single extended object rather than decomposed into multiple sources. Figure 4 shows the rel-

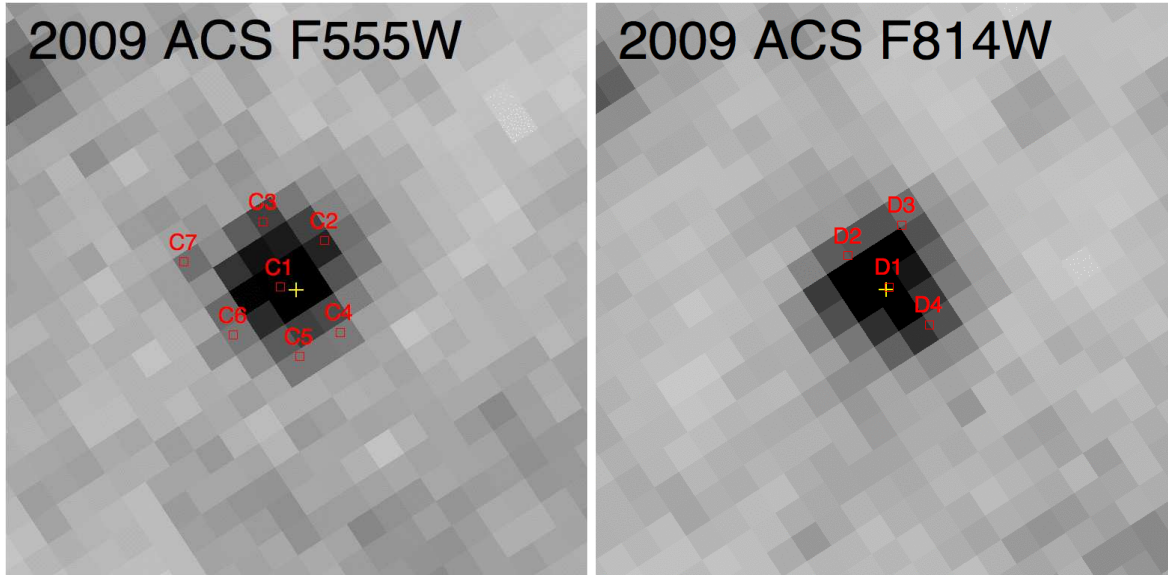


Figure 4. ACS images ($1''0$ square, North up) from 2009 (F555W and F814W, bottom) centered on the estimated position of ASASSN-16fq (yellow cross). The labeled red squares show the positions of DOLPHOT sources reported in Table 1 where the central source (C1-D1) is the brightest.

evant region of each ACS image and how it has been decomposed into the sources reported in Table 1. The HSC magnitudes agree well (~ 0.1 mag) with our results for the F435W, F555W and F658N filters. The difference is much larger for F814W, where DOLPHOT has found two sources (D1 and D2) of similar flux. The summed flux of these two sources, corresponding to 22.74 mag, agrees with the HSC flux.

We also analyzed the WFC3 images with DOLPHOT, where these are the images that best sample the PSF ($0''.04$ pixels rather than the $0''.05$ scale of ACS) and likely produce the most reliable source decomposition. We identified the sources on the *F814W* image and then obtained photometry for the *F555W* and *F814W* images simultaneously. The sources identified by DOLPHOT are shown in Figure 5 and their measured magnitudes are reported in Table 1. The position of ASASSN-16fq was again determined by aligning the WFC3 F814W image to the ACS F814W image.

The photometry reported in Table 1 is not fully consistent given the reported uncertainties. This is not very surprising given that the source appears to be a blend of multiple sources with a decomposition that is not unique under changes in the instrument, camera and filter. We tested running DOLPHOT simultaneously on the ACS and WFC3 F814W images, using a single drizzled WFC3 image for source detection. We found systematic offsets of 0.1-0.2 mag between sources as measured on the ACS and WFC3 images. For isolated point sources, the differences should be much smaller (a few times 0.01 mag in tests with SYNPHOT). However, even with the source positions fixed, the flux estimates for the blended sources likely depend in detail on the sub-pixel scale model of the PSF in each frame.

We again used difference imaging to search for evidence that the differences between the ACS and WFC3 magnitudes could be explained by variability. We focused on the F814W filter, where a red supergiant exploding as a Type II

SN should contribute the most flux. As shown in Figure 6, there are no significant residuals after using HOTPANTS to scale and subtract the two images. As with the similar test on the WFCP2 F606W images above, there is no evidence in the difference image for any variability.

We also searched the archival Spitzer data for sources related to the progenitor following the procedures of Khan et al. (2015b). We used the ISIS (Alard & Lupton 1998) difference imaging package to align the Spitzer images of a sub-region centered on ASASSN-16fq. Many of the images had an artifact passing close to the SN, so we combined the epochs either missing the artifact or where the artifact avoids its location to build a reference image. We then produced differenced images to search for variability. We also differenced the 3.5 and $4.5\mu\text{m}$ reference images to search for dusty stars. In such a “wavelength difference” image, the normal stars all vanish to leave only stars with significant hot dust emission because they all have a common “Rayleigh-Jeans” spectral energy distribution (SED) (Khan et al. 2010). We found no evidence for mid-IR variability or hot dust emission. There is no mid-IR source at the position of the progenitor. Our best estimates of the 3σ upper limits on the 3.6, 4.5, 5.8 and $8.0\mu\text{m}$ fluxes of any source at the position of the progenitor are 15.9, 15.7, 13.3 and 11.4 mag, respectively. The shorter wavelength limits correspond to $\nu L_\nu \lesssim 10^5 L_\odot$ (at 1σ), and provide no strong constraints given the HST photometry.

Clearly with the source blending and the differences between the results for the various cameras we cannot precisely determine the properties of the progenitor or the amount of extinction. Our goal is simply to provide constraints on the progenitor luminosity that can be translated into rough constraints on the stellar mass. ASASSN-16fq is a Type IIP SN, and all progenitors of Type IIP SN with constrained stellar temperatures have been red supergiants (see Smartt 2015) with stellar temperatures of order $T_* = 3500$ K. Higher tem-

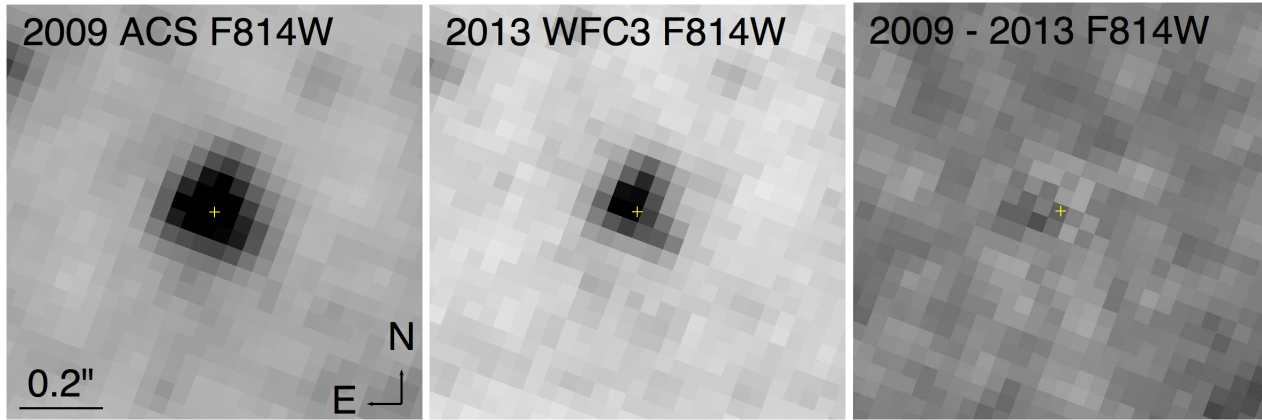


Figure 6. No evidence for variability at F814W. The $1''$ square (North up) panels show the ACS (left) and WFC3 (middle) F814W images from 2009 and 2013, respectively, along with the HOTPANTS difference image (right) between them. The position of the progenitor candidate for ASASSN-16fq is marked with a yellow cross in all three panels. In the difference image, sources which are brighter in the ACS image appear dark while those that are brighter in the WFC3 image appear white.

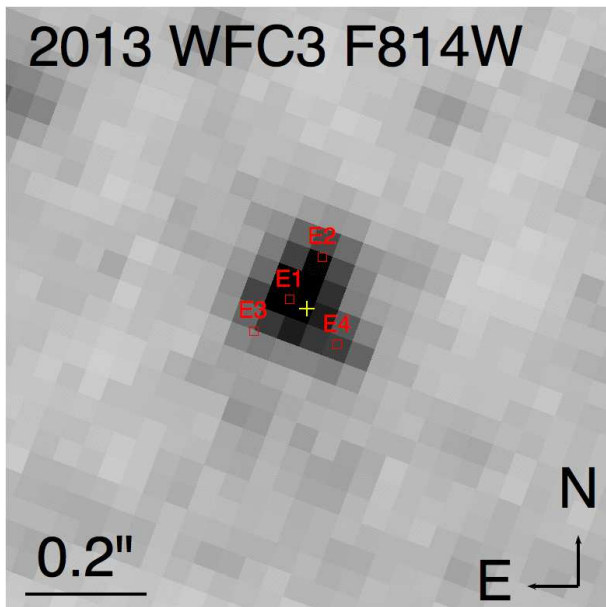


Figure 5. WFC3 F814W image ($1''$ square, North up) from 2013 centered on the estimated position of ASASSN-16fq (yellow cross). The labeled red squares show the positions of DOLPHOT sources reported in Table 1 where the central source (E1) is the brightest.

peratures of order $T_* = 6000$ K have been observed for the progenitors of Type IIb SNe (e.g., SN 2011dh, Maund et al. 2011). Finally, we must note the still higher temperature progenitor of the Type IIpec SN 1987A, a blue supergiant with $T_* \simeq 16000$ K and $L_* \simeq 10^{5.0} L_\odot$ (see the review by Arnett et al. 1989). All available evidence is that ASASSN-16fq is a normal Type IIP SN where we should only consider the lowest temperature ($T_* = 3500$ K), but we will present parallel results for $T_* = 6000$ K and comment on the consequences of still higher progenitor temperatures.

Rodríguez et al. (2016, in preparation) modeled the early, near-UV/optical/near-IR photometry (from *Swift*,

LCOGT 1m, the Iowa Observatory 0.5m, and the REM 0.6m) and photospheric expansion velocities of ASASSN-16fq (obtained from optical spectra obtained with FLWO 1.5m+FAST and MDM 2.4m+OSMOS) following Pejcha & Prieto (2015). This phenomenological model describes the multicolor light curves and photospheric velocity evolution of normal Type II SNe, decoupling changes in effective temperature from changes in the photospheric radius at different epochs since explosion. These fits lead to an estimated explosion time of $JD = 2457532.2 \pm 2.0$ days, a total extinction (including Galactic) of $E(B - V) = 0.53 \pm 0.02$ mag, and a distance modulus of 29.72 ± 0.44 mag. This distance estimate of 8.8 ± 1.8 Mpc is consistent with our adopted value of 10.62 Mpc. For roughly estimating the properties of the progenitor, we will assume either Galactic $E(B - V) = 0.03$ or $E(B - V) = 0.53$ of foreground extinction. The results assuming circumstellar extinction would be moderately different (see Kochanek et al. 2012a for a discussion of this issue).

We corrected the photometry for the assumed amount of foreground extinction and then used the DUSTY dust radiation transport code (Ivezić & Elitzur 1997, Ivezić et al. 1999, Elitzur & Ivezić 2001) combined with Castelli & Kurucz (2004) model atmospheres of solar metallicity and embedded in a Monte Carlo Markov Chain (MCMC) driver to match the model to the data (see Adams & Kochanek 2015, Adams et al. 2016 for details). For the experiments we carry out here, much of this machinery is not necessary but can be trivially applied to the problem. For a fixed stellar temperature and foreground extinction we determined the stellar luminosity based on one of the broad band ACS or WFC3 total or brightest component magnitudes. The brightest, total broad band magnitudes (those from ACS) were used as 1σ upper limits on the luminosity unless the magnitude was being used to determine the luminosity. In essence, we will not attempt to extract any color information from the photometry, but no model can be significantly brighter than the brightest observed ACS/WFC3 broad band magnitudes.

Figure 7 shows the “SED” of the source combining the

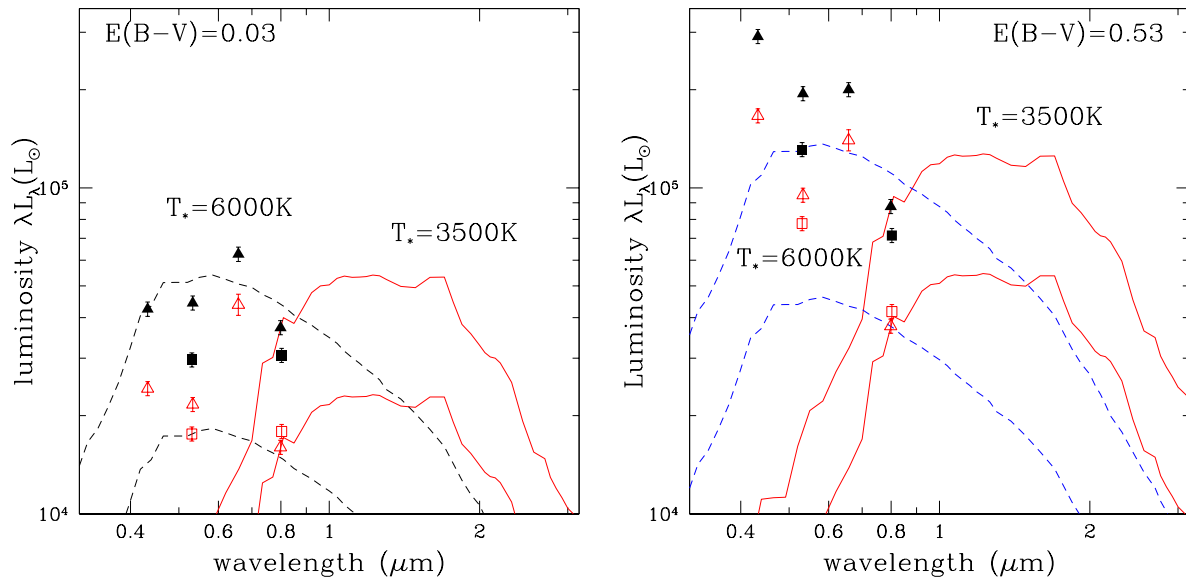


Figure 7. Spectral energy distributions with low ($E(B - V) = 0.03$, left) and high ($E(B - V) = 0.53$, right) extinction. The open (filled) squares show the WFC3 photometry for the brightest source (total of all sources) in Table 1. The open (filled) triangles show the ACS photometry for the brightest source (total of all sources) in Table 1. The solid red (dashed blue) curves show the $T_* = 3500$ K ($T_* = 6000$ K) stellar SEDs with the lowest and highest luminosities that fit one of the broad band photometric points and do not significantly exceed the brightest, total broad band fluxes (the total ACS fluxes for the broad band filters).

ACS and WFC3 photometry. All else being equal and ignoring the narrow band F658N photometry, the luminosity estimate will vary by roughly a factor of two between a model based on the fluxes of the brightest components (A1-E1) and the summed fluxes of all the components. For example, using $T_* = 3500$ K and Galactic extinction, only models normalized at I-band (F814W) are also consistent with the relevant upper limits. They have luminosities in the range from $L_* = 10^{4.5}$ to $10^{4.9} L_\odot$. Essentially, the cool models are too luminous for the observed F814W fluxes if they are normalized at shorter wavelengths. For the hotter $T_* = 6000$ K model, all permutations are allowed, and they have luminosities spanning a very similar range from $L_* = 10^{4.5}$ to $10^{4.8} L_\odot$. At the hotter temperature, the stellar SED is not dropping rapidly in the bluer bands and so it is easier to be consistent with all the constraints. When we raise the extinction to $E(B - V) = 0.53$, the changes in the results are modest. For $T_* = 3500$ K, only the F814W normalizations are again allowed but with a shift to moderately higher luminosities of $10^{4.8}$ to $10^{5.2} L_\odot$. For $T_* = 6000$ K the F814W and F555W normalizations are allowed and they have the same luminosity range as for the $T_* = 3500$ K models.

A hot star, albeit one still hotter than the progenitor of SN 1987A, might also explain the discrepant F658N magnitudes as H α emission from an associated HII region. With the large $E(B - V) = 0.53$ extinction correction, the implied SED also rises rapidly to shorter wavelengths as might be expected for a hot star. Since the SED rises rapidly to shorter wavelengths, these hot star models are very luminous, with $L_* = 10^{5.5}$ to $10^{6.0} L_\odot$ for $T_* = 16000$ K and still higher luminosities for higher temperatures. We will not consider this possibility further, although it would make ASASSN-16fq a unique and fascinating new example of the SN phenomenon were it to prove to be true.

If we use the endpoints of the PARSEC (Bressan et al. 2012) isochrones to map luminosities into masses, luminosities of $L_* = 10^{4.5}$, $10^{4.8}$, $10^{4.9}$ and $10^{5.2} L_\odot$ translate into initial masses of $M_* \simeq 8.6$, 11.2, 11.6 and $17 M_\odot$. Since the higher luminosity limits correspond to the cases normalized by the total flux of all the detected sources rather than just that of the brightest source found by DOLPHOT, they should probably be treated as upper limits. In short, despite the chaotic nature of the photometry, the progenitor of ASASSN-16fq was probably a red supergiant with an initial mass of 8-12 M_\odot . This estimate of the mass range is fairly robust to changes in temperature, unless the star is significantly hotter than expected ($T_* > 6000$ K), and holds for a fairly broad range of extinctions. It probably does require that some of the blended stars are significantly hotter and bluer, which would be natural if they are also younger.

3 LBT AND THE VARIABILITY OF THE PROGENITOR

As part of the LBT search for failed SN (Kochanek et al. 2008, Gerke et al. 2015), NGC 3627 was observed sixteen times in the U, B, V and R-bands between 4 May 2008 and 7 February 2016. NGC 3627 lies on chip 3 of the Large Binocular Camera (LBC, Giallongo et al. 2008) images. The LBT data are analyzed using the ISIS (Alard & Lupton 1998) difference imaging package. First, all the images are aligned to a common R-band astrometric reference image. The best images (noise, resolution and quality) for each band are combined to make a reference image. These reference images are astrometrically and photometrically calibrated based on SDSS stars (Pier et al. 2003, Ivezić et al. 2007, Ahn et al. 2012) with the SDSS ugriz photometry trans-

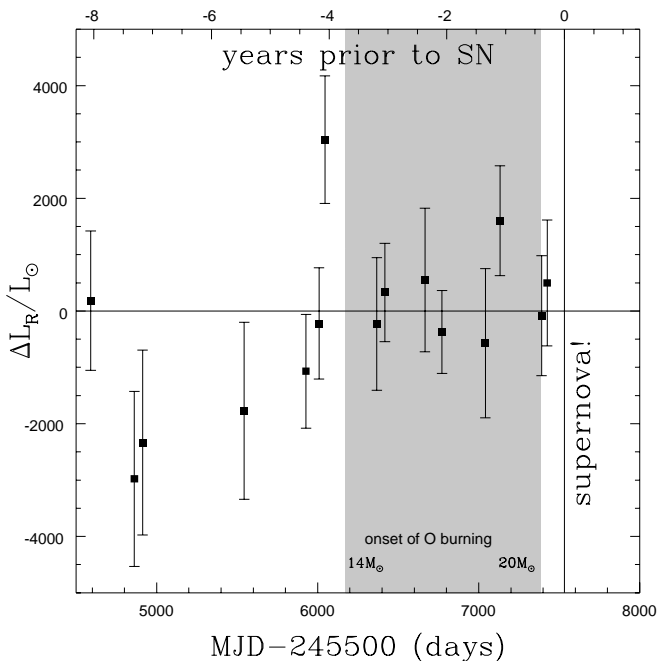


Figure 8. R-band progenitor variability prior to the supernova relative to the error-weighted mean. The luminosities are not corrected for extinction. The gray band shows the times for the commencement of core oxygen burning for stars with initial mass of $14M_{\odot}$ (left edge) to $20M_{\odot}$ (right edge) from Sukhbold & Woosley (2014) (see Figure 1 for the full mass dependence).

formed to UBV_R Vega magnitudes using the relations in Jordi et al. (2006). The reference images are then subtracted from the individual epochs to leave only the variable flux between the reference image and the individual epochs. Since the reference image is constructed from images spanning the monitoring period, source fluxes in the reference image roughly correspond to the mean fluxes.

We cannot measure the absolute flux of the progenitor in the LBT images due to crowding. However, the subtracted images are not crowded and we can easily constrain the variability of the progenitor. For this purpose, the uniformity of the data and the well-sampled PSF makes the ground-based LBT data superior to the archival HST data. Although variability is seen in none of the bands, we focus only on the R-band data, which is both deeper and of higher quality. Table 2 provides the difference in the R-band luminosity relative to the error-weighted mean of all the epochs. The conversion between the R-band (νL_{ν}) luminosity and counts is $3.26L_{\odot}/\text{count}$ and no correction for extinction has been applied.

As seen in Figure 8 and Table 2, there is no statistically significant evidence for variability from the progenitor. The root-mean-square (RMS) of the variability is $1505L_{\odot}$ as compared to a mean square uncertainty of $1204L_{\odot}$. Subtracting in quadrature, this implies variability at an RMS level of $900L_{\odot}$. Because the RMS is so close to the level of the uncertainties, these should be regarded as upper limits on the variability rather than detections. If we fit a linear trend, the slope is $(220 \pm 133)L_{\odot} \text{ year}^{-1}$ with $\chi^2 = 16.4$ for 13 degrees of freedom. If we rescale the uncertainties to make the χ^2 per degree of freedom unity, this becomes

$(291 \pm 149)L_{\odot} \text{ year}^{-1}$. If we adopt an R-band luminosity of $\nu L_{\nu} = 10^{4.3}L_{\odot}$, the RMS variability is $< 4.5\%$ and the limit on the slope is $(1.4 \pm 0.7)\% \text{ year}^{-1}$. This luminosity estimate is the logarithmic average of the Galactic extinction-corrected ACS and WFC F814W and F555W C1, D1 and E1 source luminosities. The absolute scale of these luminosities is subject to distance uncertainties and extinction corrections, but the fractional variability is independent of both.

Figure 8 shows the relation of the LBT epochs to nuclear burning phases with a gray band bracketing the onset of core oxygen burning for models with $14M_{\odot} < M < 20M_{\odot}$ from Sukhbold & Woosley (2014), where the full mass dependence is shown in Figure 1. More or less independent of mass, the LBT data samples the last phases of carbon shell burning, the neon burning phase (not shown), core oxygen burning, and the initial phases of shell oxygen burning. Since the two points that drive the apparent slope in the luminosity evolution probably lie in the shell carbon burning phase, the variability in the later burning phases is even smaller than the overall limits given above.

4 DISCUSSION

We have clearly identified a counterpart to ASASSN-16fq in archival HST data. Unfortunately, our constraints on the properties of the progenitor are far from satisfactory, presumably due to the blending of multiple stars with the progenitor even at the resolution of HST. However, for a broad range of reasonable assumptions about its temperature and the amount of extinction, its properties are consistent with a lower-mass ($8\text{--}12M_{\odot}$) red supergiant. The data almost certainly require an upper mass limit of $M_{*} \lesssim 17M_{\odot}$ that matches the mass limit associated with the red supergiant problem (Smartt et al. 2009) or the more general problem of missing higher mass SN progenitors originally identified by Kochanek et al. (2008). The only real escape from this conclusion is to give the progenitor a far higher than expected temperature, but this option quickly drives the progenitor luminosity to be extraordinarily high. While we view this possibility as unlikely, it would make the progenitor of ASASSN-16fq far more remarkable than simply making it a garden variety red supergiant of modest mass. Observations either with the LBT or HST once the SN has faded will have no difficulty making accurate photometric measurements of the progenitor.

Table 3 summarizes the available information on the variability of SN progenitors beyond the large outbursts probed by Ofek et al. (2014), Bilinski et al. (2015) and Strotjohann et al. (2015). Information is available for the Type Ipec SN 1987A (photographic, Plotkin & Clayton 2004), the Type IIb SN 1993J (V-band, Cohen et al. 1995), the Type IIP SN 2008cn (V-band, Elias-Rosa et al. 2009, Maund et al. 2015), the Type IIb SN 2011dh (R-band, Szczygiel et al. 2012) and the Type IIP SN 2013ej (I-band, Fraser et al. 2014) in addition to ASASSN-16fq. Based on the review of Smartt (2009), we adopt progenitor masses of $14\text{--}20M_{\odot}$ for SN 1987A and $15M_{\odot}$ for SN 1993J. We use an upper limit of $< 16M_{\odot}$ for SN 2008cn following Maund et al. (2015), $(13 \pm 3)M_{\odot}$ for SN 2011dh following Maund et al. (2011), and $8\text{--}15.5M_{\odot}$ for SN 2013ej (Fraser et al. 2014).

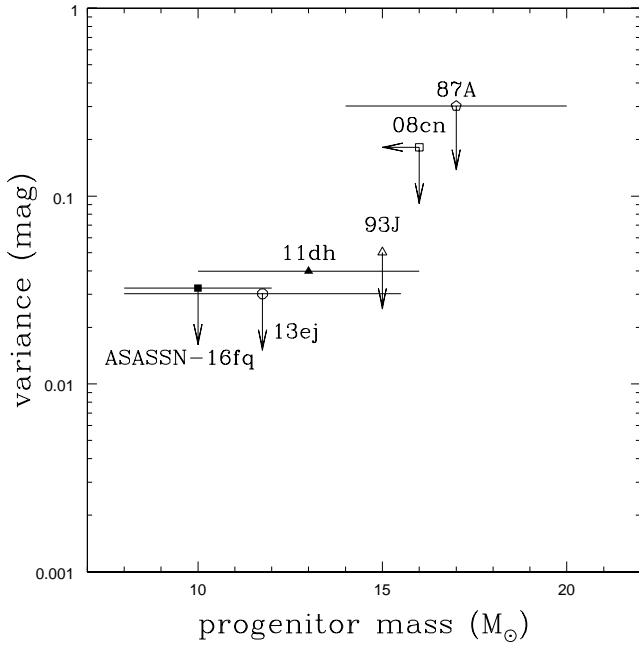


Figure 9. (Left) Magnitude variance of the 6 SN progenitors as a function of their estimated mass. The variance in the progenitor’s flux is a measure of any “random” variability of the progenitor. The time period over which the variance was estimated varies between the SN (see Figure 1).

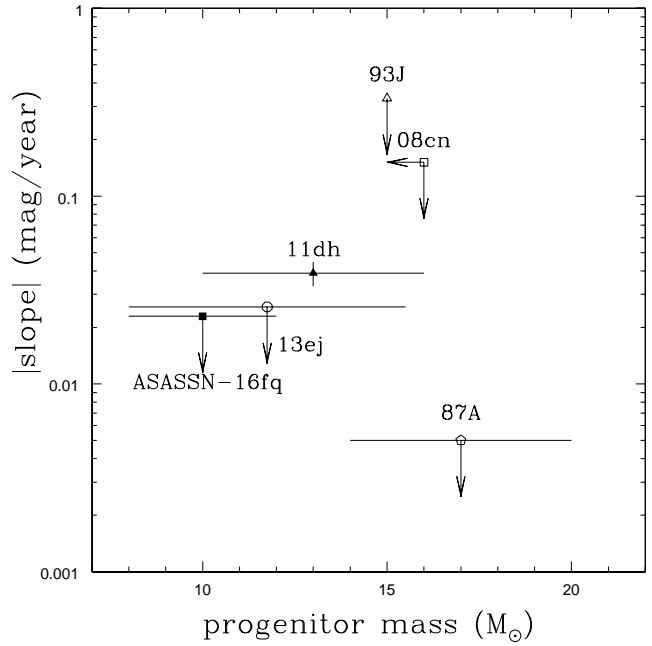


Figure 10. (Right) Absolute values of the linear luminosity slopes of the 6 SN progenitors as a function of their estimated mass. The slope of the progenitor’s flux is a measure of any “steady” variability of the progenitor. For the SN where we have only upper limits, the limit is drawn at the absolute value of the slope plus the uncertainty in the slope. The time period over which the slope was estimated varies between the SN (see Figure 1).

We use our estimate of $8\text{--}12M_{\odot}$ from §2 for ASASSN-16fq. We also report the time period spanned by the variability data and (roughly) the corresponding nuclear burning phases based on Figure 1. The data for SN 1987A, SN 1993J, SN 2008cn and SN 2013ej probably only sample the carbon shell burning phase. The LBT data for SN 2011dh, like that for ASASSN-16fq, probably samples the last phases of carbon shell burning through the early phases of oxygen shell burning.

We can characterize the “random,” “steady,” and “outburst” variability of these SN progenitors. Limits on the random variability are illustrated by the “Var” estimates of the intrinsic variability as a function of the progenitor mass in Figure 9. The variance “Var” is estimated by subtracting the mean of the reported photometric uncertainties ($\langle \text{Err} \rangle$) from the root mean square (RMS) of the light curve, ($\text{Var} = (\text{RMS}^2 - \langle \text{Err} \rangle^2)^{1/2}$). The intrinsic variability is defined to be zero if the mean errors exceed the RMS, as is the case for SN 2013ej and the Maund et al. (2015) results for SN 2008cn. These quantities are reported in Table 3. Limits on the steady variability are illustrated in Figure 10 by the estimates of the linear luminosity slopes as a function of progenitor mass. The upper limits used for all but SN 2011dh are drawn at the absolute value of the slope plus the error estimate. The slope estimates and the goodness of fit are included in Table 3.

Of these SN, only SN 2011dh is clearly variable, but with the small number of epochs available to Szczygiel et al. (2012) it is also possible to interpret it as ellipsoidal vari-

ability given the binary models for the progenitor system by Benvenuto et al. (2013). For comparison, typical slopes estimated from the end points of stellar evolution models are 10^{-3} to 10^{-4} mag/year (e.g., Schaller et al. 1992, Heger & Langer 2000). The limit on the slope for SN 1987A is by far the tightest due to the long time span of the data. Obviously, these systems are heterogeneously selected and sample different final burning phases (see Figure 1), but they also appear to be the only published progenitors with adequate data to test for these lower levels of variability.

We can characterize outbursts by adding Gaussian bursts in luminosity (quadratic in magnitude) defined by a peak luminosity L_{peak} and a burst FWHM t_{peak} to the light curves of all the sources in Table 3 except SN 1987A. We allow the outbursts during an eruption time corresponding to the last t_{out} before the SN. We normalize the available light curves to have a χ^2 per degree of freedom, N_{dof} , of at most unity (i.e. ignoring the variability of SN 2011dh) when fit as having a constant flux. We then add model outbursts at random times and conservatively define detection to be when the χ^2 for fitting the “fake” data containing an outburst as having a constant flux exceeds the larger of $2N_{dof}$ and $N_{dof} + 4$. Figure 11 shows the results, quantified as the detection probability per SN, P_d , for peak outburst luminosities of $M_R = -6, -8, -10$ and -12 mag, corresponding to $\lambda L_{\lambda} \simeq 10^{4.0}, 10^{4.8}, 10^{5.6}$ and $10^{6.4} L_{\odot}$. The detection probabilities can then be converted to 90% confidence limits on the number of outbursts per SN as

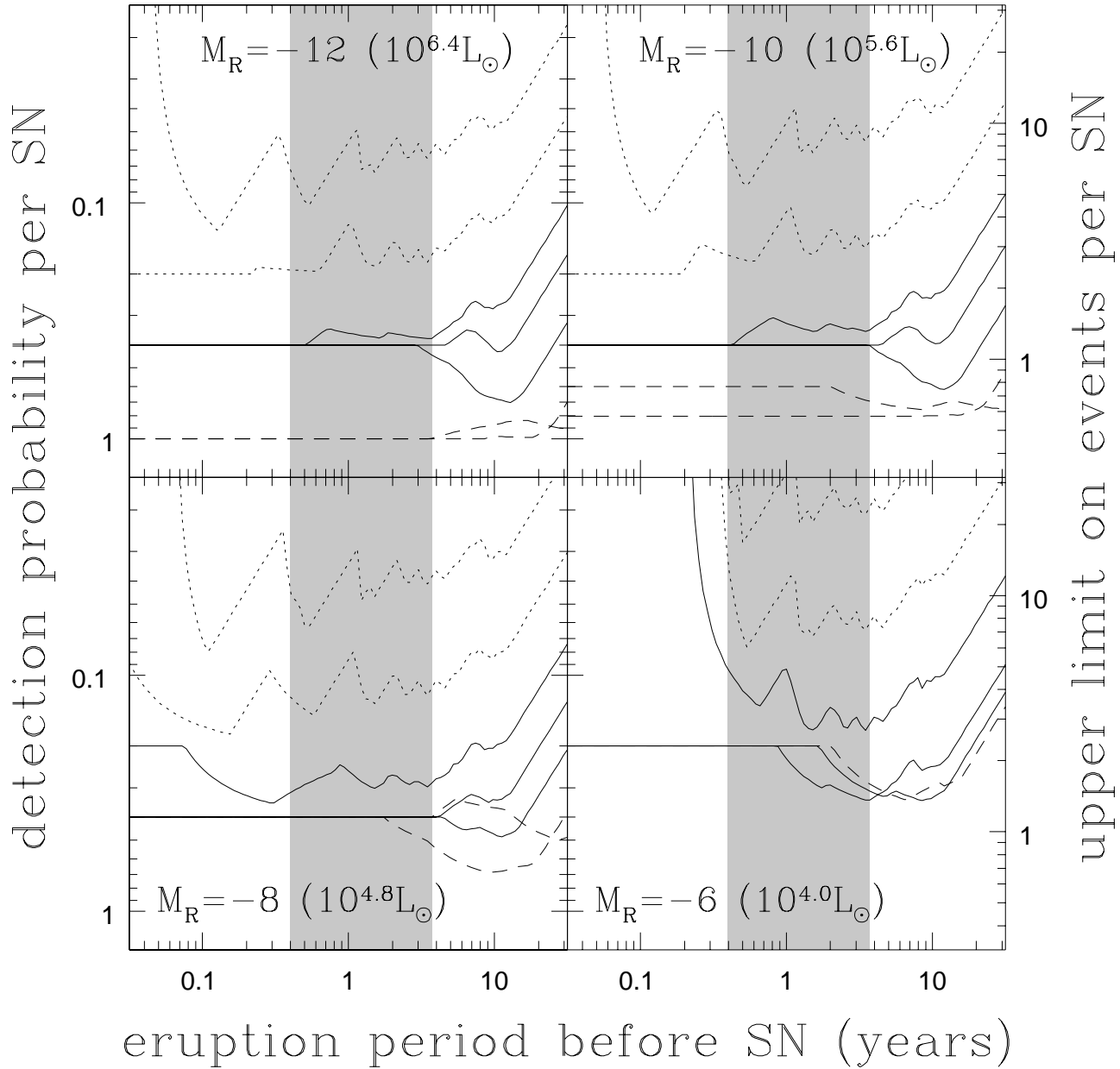


Figure 11. Outburst detection probabilities (P_d , left scale) and 90% confidence upper limits on the number of outbursts per SN (N_{out} , right scale) as a function of the period t_{out} over which eruptions can occur prior to the SN. The panels show the results for different peak luminosities from $M_R = -12$ (top left) down to $M_R = -6$ mag (bottom right) where the associated luminosities are λL_λ at R-band. The curves correspond to logarithmically spaced outburst FWHM of $t_{peak} = 0.032$ (highest, dotted), 0.1 (dotted), 0.32 (solid), 1.0 (solid), 3.2 (solid), 10.0 (dashed) and 32 (usually lowest, dashed) years. As in Figure 8, the shaded region shows the time before collapse for the onset of core oxygen burning in the $14M_\odot$ and $20M_\odot$ models (see Figure 1). The limit on the number of N_{out} outbursts and the detection probability P_d are related by $N_{out} = 2.3(N_{SN}P_d)^{-1}$ for the $N_{SN} = 5$ SN excluding SN 1987A.

$$N_{out} < \frac{2.30}{N_{SN}P_d} = 0.46P_d^{-1} \quad (1)$$

where $N_{SN} = 5$ since we have excluded SN 1987A from the analysis. The rate of eruptions during the eruption period is then $r_{out} = N_{out}/t_{out}$.

The general pattern of the detection probabilities P_d in Figure 11 is relatively easy to understand. Short outbursts become increasingly difficult to detect because of the

finite temporal sampling of the data. Long outbursts ultimately become difficult to detect because they show no time variability over the finite temporal extent of the data (although for sufficiently bright transients the luminosity would be incompatible with any progenitor). The results for long outbursts eventually correspond to the slope limits of Figure 10. The sensitivity is highest for eruption periods extending to roughly 10 years because SN 1993J, SN 2008cn

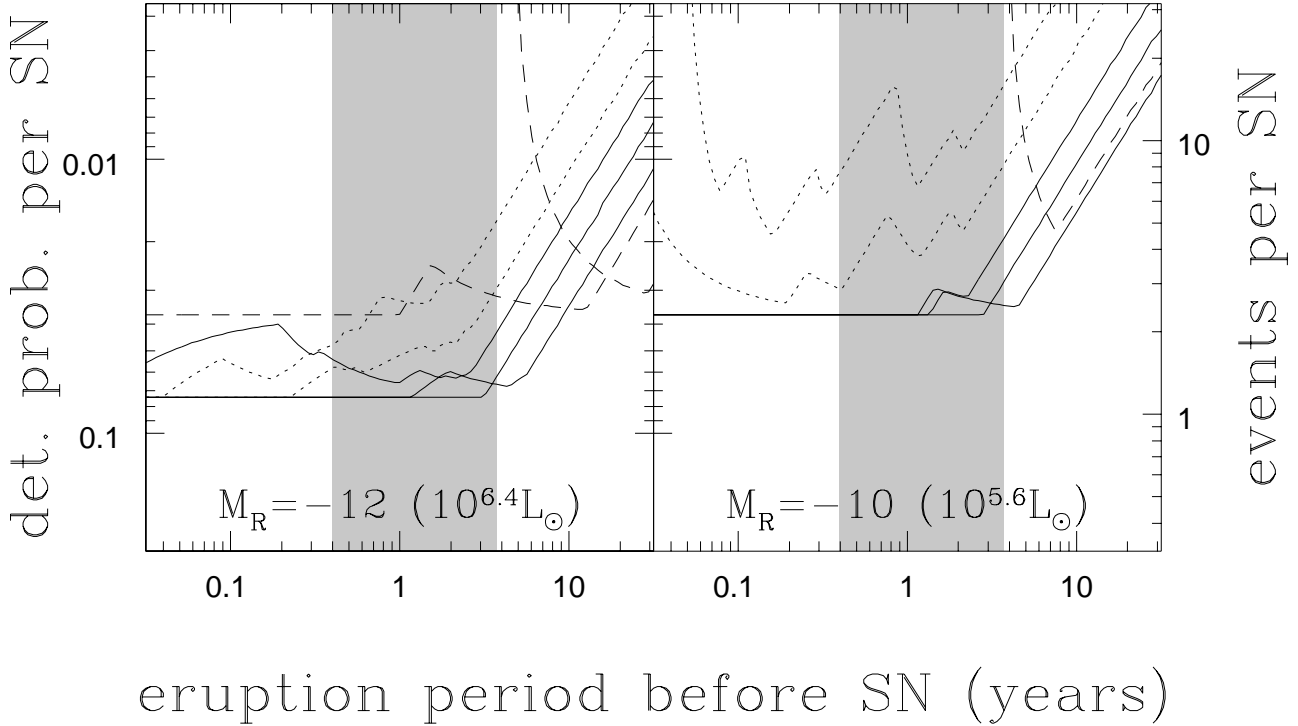


Figure 12. Outburst detection probabilities (left scale) and 90% confidence upper limits on the number of outbursts per SN (right scale) as a function of the period over which eruptions can occur prior to the SN for the PTF data on Type IIb SN progenitors considered by Strotjohann et al. (2015). The format is the same as in Figure 11, but we only show the results for $M_R = -10$ and -8 mag where there is some overlap with the sensitivities shown in Figure 11. The curves correspond to logarithmically spaced outburst FWHM of $t_{peak} = 0.032$ (highest, dotted), 0.1 (dotted), 0.32 (solid), 1.0 (solid), 3.2 (solid), 10.0 (dashed) and 32 (usually lowest, dashed) years. The PTF sample is better for brighter transients (more SN with better temporal coverage) and worse for fainter transients (insufficient depth). As in Figure 8, the shaded region shows the time before collapse for the onset of core oxygen burning in the $14M_\odot$ and $20M_\odot$ models (see Figure 1). The limit on the number of N_{out} outbursts and the detection probability P_d are related by $N_{out} = 2.3(N_{SN}P_d)^{-1}$ for the $N_{SN} = 27$ SN in the Strotjohann et al. (2015) sample.

and SN 2013ej only contribute on these time scales. For the shortest eruption periods (t_{out}), only SN 2011dh contributes, and for long eruption periods, there is no information outside the last roughly 10 years before the SN.

Figure 12 shows outburst limits computed in the same manner for the sample of 27 Type IIb SN considered by Strotjohann et al. (2015) for comparison. Ofek et al. (2014) and Strotjohann et al. (2015) provide 5σ R-band luminosity limits, L_{PTF} , for 15 day bins of the data, each containing a variable number, N_{PTF} , of epochs. For simplicity, we simply spread the reported number of epochs uniformly over their 15 day bin (with temporal spacings of $1/2 : 1 : 1 \cdots 1 : 1 : 1/2$ over the bin), each with a (1σ) uncertainty per epoch of $L_{PTF}N_{PTF}^{1/2}/5$. We can then apply our formalism with only minor ambiguities for very short time scale ($t_{peak} \lesssim 15$ day) outbursts. Figure 12 shows the results for the Strotjohann et al. (2015) sample at $M_R = -12$ and -10 mag. The Type IIc sample considered by Ofek et al. (2014) has even less sensitivity to low luminosity outbursts because the typical SN is more distant and there are fewer SN in the sample.

As we can see from comparing Figures 11 and 12, the PTF sample is more sensitive to very luminous outbursts and far less sensitive to outbursts closer to the progenitor

luminosity. This is simply because, relative to the sample in Table 3, the PTF data has more continuous, but very shallow, coverage of a larger number of SN. The rate limits of the two samples cross near peak luminosities of $M_R = -12$ mag ($\lambda L_\lambda \simeq 10^{6.4} L_\odot$), where the relative sensitivity depends on the burst duration. By $M_R = -10$ mag ($\lambda L_\lambda \simeq 10^{5.6} L_\odot$), the deeper data we use here is more sensitive independent of the outburst duration. The PTF data has negligible sensitivity to the fainter $M_R = -8$ and -6 mag outbursts.

In essence, the two approaches are complimentary. SN surveys like PTF will better constrain the rates of high luminosity, shorter transients – they will generally have larger numbers of SN observed with higher cadence. However, even with the co-addition of data, SN surveys simply lack the sensitivity to probe variability significantly below ~ 10 times the luminosity of the progenitor stars. Deep monitoring data, like that from our LBT survey, are sensitive to very low levels of variability (down to $\sim 1\%$ of the progenitor luminosity, Figure 8), but are limited by the SN rate in nearby galaxies (~ 1 year) and the lower cadence of any monitoring project on large telescopes.

SN surveys like PTF are also largely limited to studying the relationships between outburst and SN properties, as done by Ofek et al. (2014), because most of the SN will be

too distant for measurements of the progenitor properties. Any survey which can measure variability on the scale of the progenitor luminosity or fainter can, by definition, also determine the properties of the progenitor. As a result, studies like the LBT survey (Kochanek et al. 2008, Gerke et al. 2015) are better suited to studying the relationship between outbursts and progenitors. An obvious next step is to systematically analyze the variability of all the SN progenitors in the LBT survey data, which will provide a relatively homogeneous, volume-limited sample, rather than the heterogeneous sample represented by Table 3.

ACKNOWLEDGMENTS

We thank A. Dolphin for his advice regarding DOLPHOT. CSK, KZS, JSB, SMA and TWSH are supported by NSF grants AST-1515876 and AST-1515927. BJS is supported by NASA through Hubble Fellowship grant HF-51348.001 awarded by the Space Telescope Science Institute, which is operated by the Association of Universities for Research in Astronomy, Inc., for NASA, under contract NAS 5-26555. TW-SH is supported by the DOE Computational Science Graduate Fellowship, grant number DE-FG02-97ER25308. TS is partly supported by NSF grant PHY-1404311 to J. Beacom. This work was partly supported by the European Union FP7 program through ERC grant number 320360. Support for JLP is provided in part by FONDECYT through the grant 1151445 and by the Ministry of Economy, Development, and Tourism's Millennium Science Initiative through grant IC120009, awarded to The Millennium Institute of Astrophysics, MAS. SD is supported by the Strategic Priority Research Program "The Emergence of Cosmological Structures" of the Chinese Academy of Sciences (Grant No. XDB09000000) and NSFC project 11573003. Some of the observations were carried out using the LBT at Mt Graham, AZ. The LBT is an international collaboration among institutions in the United States, Italy, and Germany. LBT Corporation partners are the University of Arizona on behalf of the Arizona university system; Istituto Nazionale di Astrofisica, Italy; LBT Beteiligungsgesellschaft, Germany, representing the Max-Planck Society, the Astrophysical Institute Potsdam, and Heidelberg University; the Ohio State University; and The Research Corporation, on behalf of the University of Notre Dame, University of Minnesota, and University of Virginia. This work is based in part on observations made with the Spitzer Space Telescope, which is operated by the Jet Propulsion Laboratory, California Institute of Technology under a contract with NASA, and in part on observations made with the NASA/ESA Hubble Space Telescope obtained at the Space Telescope Institute, which is operated by the Association of Universities for Research in Astronomy, Inc., under NASA contract NAS 5-26555. Some observations were obtained from the Hubble Legacy Archive, which is a collaboration between the Space Telescope Science Institute (STScI/NASA), the Space Telescope European Coordinating Facility (ST-ECF/ESA) and the Canadian Astronomy Data Centre (CADK/NRC/CSA).

REFERENCES

- Abbott, B. P., Abbott, R., Abbott, T. D., et al. 2016, *Physical Review Letters*, 116, 061102
- Adams, S. M., & Kochanek, C. S. 2015, *MNRAS*, 452, 2195
- Adams, S. M., Kochanek, C. S., Prieto, J. L., et al. 2016, *MNRAS*, 460, 1645
- Ahn, C. P., Alexandroff, R., Allende Prieto, C., et al. 2012, *ApJS*, 203, 21
- Alard, C., & Lupton, R. H. 1998, *ApJ*, 503, 325
- Arnett, W. D., Bahcall, J. N., Kirshner, R. P., & Woosley, S. E. 1989, *ARA&A*, 27, 629
- Belczynski, K., Holz, D. E., Bulik, T., & O'Shaughnessy, R. 2016, arXiv:1602.04531
- Benvenuto, O. G., Bersten, M. C., & Nomoto, K. 2013, *ApJ*, 762, 74
- Bilinski, C., Smith, N., Li, W., et al. 2015, *MNRAS*, 450, 246
- Bock, G., Dong, S., Kochanek, C.S., et al. 2016, *The Astronomer's Telegram*, 9091
- Bressan, A., Marigo, P., Girardi, L., et al. 2012, *MNRAS*, 427, 127
- Brown, J. M., & Woosley, S. E. 2013, *ApJ*, 769, 99
- Cao, Y., Kasliwal, M. M., Arcavi, I., et al. 2013, *ApJL*, 775, L7
- Castelli, F., & Kurucz, R. L. 2004, arXiv:astro-ph/0405087
- Couch, S. M., & Ott, C. D. 2015, *ApJ*, 799, 5
- Clausen, D., Piro, A. L., & Ott, C. D. 2015, *ApJ*, 799, 190
- Cohen, J. G., Darling, J., & Porter, A. 1995, *AJ*, 110, 308
- Dalcanton, J. J., Williams, B. F., Seth, A. C., et al. 2009, *ApJS*, 183, 67
- Dolence, J. C., Burrows, A., & Zhang, W. 2015, *ApJ*, 800, 10
- Dolphin, A. E. 2000, *PASP*, 112, 1383
- Eldridge, J. J., Fraser, M., Smartt, S. J., Maund, J. R., & Crockett, R. M. 2013, *MNRAS*, 436, 774
- Elias-Rosa, N., Van Dyk, S. D., Li, W., et al. 2009, *ApJ*, 706, 1174
- Elias-Rosa, N., Van Dyk, S. D., Li, W., et al. 2011, *ApJ*, 742, 6
- Elitzur, M., & Ivezić, Ž. 2001, *MNRAS*, 327, 403
- Ertl, T., Janka, H.-T., Woosley, S. E., Sukhbold, T., & Ugliano, M. 2016, *ApJ*, 818, 124
- Filippenko, A. V. 1997, *ARA&A*, 35, 309
- Folatelli, G., Van Dyk, S. D., Kuncarayakti, H., et al. 2016, arXiv:1604.06821
- Foley, R. J., Berger, E., Fox, O., et al. 2011, *ApJ*, 732, 32
- Fraser, M., Maund, J. R., Smartt, S. J., et al. 2012, *ApJL*, 759, L13
- Fraser, M., Magee, M., Kotak, R., et al. 2013, *ApJL*, 779, L8
- Fraser, M., Maund, J. R., Smartt, S. J., et al. 2014, *MNRAS*, 439, L56
- Gal-Yam, A. 2012, *Science*, 337, 927
- Gerke, J. R., Kochanek, C. S., & Stanek, K. Z. 2015, *MNRAS*, 450, 3289
- Giallongo, E., Ragazzoni, R., Grazian, A., et al. 2008, *AAP*, 482, 349
- Groh, J. H., Meynet, G., Georgy, C., & Ekström, S. 2013, *AAP*, 558, A131
- Heger, A., & Langer, N. 2000, *ApJ*, 544, 1016
- Ivezić, Z., & Elitzur, M. 1997, *MNRAS*, 287, 799

- Ivezić, Z., Nenkova, M., & Elitzur, M. 1999, arXiv:astro-ph/9910475
- Jennings, Z. G., Williams, B. F., Murphy, J. W., et al. 2014, *ApJ*, 795, 170
- Horiuchi, S., Beacom, J. F., Kochanek, C. S., et al. 2011, *ApJ*, 738, 154
- Humphreys, R. M., & Davidson, K. 1994, *PASP*, 106, 1025
- Ivezić, Ž., Smith, J. A., Miknaitis, G., et al. 2007, *AJ*, 134, 973
- Jerkstrand, A., Smartt, S. J., Fraser, M., et al. 2014, *MNRAS*, 439, 3694
- Jordi, K., Grebel, E. K., & Ammon, K. 2006, *AAP*, 460, 339
- Kanbur, S. M., Ngeow, C., Nikolaev, S., Tanvir, N. R., & Hendry, M. A. 2003, *AAP*, 411, 361
- Khan, R., Stanek, K. Z., Prieto, J. L., et al. 2010, *ApJ*, 715, 1094
- Khan, R., Kochanek, C. S., Stanek, K. Z., & Gerke, J. 2015, *ApJ*, 799, 187
- Khan, R., Adams, S. M., Stanek, K. Z., Kochanek, C. S., & Sonneborn, G. 2015, *ApJL*, 815, L18
- Kiewe, M., Gal-Yam, A., Arcavi, I., et al. 2012, *ApJ*, 744, 10
- Kochanek, C. S., Beacom, J. F., Kistler, M. D., et al. 2008, *ApJ*, 684, 1336
- Kochanek, C. S. 2011, *ApJ*, 743, 73
- Kochanek, C. S., Szczygiel, D. M., & Stanek, K. Z. 2011, *ApJ*, 737, 76
- Kochanek, C. S., Khan, R., & Dai, X. 2012, *ApJ*, 759, 20
- Kochanek, C. S., Szczygiel, D. M., & Stanek, K. Z. 2012, *ApJ*, 758, 142
- Kochanek, C. S. 2014, *ApJ*, 785, 28
- Kochanek, C. S. 2015, *MNRAS*, 446, 1213
- Li, W., Van Dyk, S. D., Filippenko, A. V., et al. 2006, *ApJ*, 641, 1060
- Li, W., Leaman, J., Chornock, R., et al. 2011, *MNRAS*, 412, 1441
- Lien, A., Fields, B. D., & Beacom, J. F. 2010, *PRD*, 81, 083001
- Margutti, R., Milisavljevic, D., Soderberg, A. M., et al. 2014, *ApJ*, 780, 21
- Mauerhan, J. C., Smith, N., Filippenko, A. V., et al. 2013, *MNRAS*, 430, 1801
- Maund, J. R., Smartt, S. J., Kudritzki, R. P., Podsiadlowski, P., & Gilmore, G. F. 2004, *Nature*, 427, 129
- Maund, J. R., Fraser, M., Ergon, M., et al. 2011, *ApJL*, 739, L37
- Maund, J. R., Fraser, M., Reilly, E., Ergon, M., & Mattila, S. 2015, *MNRAS*, 447, 3207
- Müller, B. 2016, arXiv:1608.03274
- O'Connor, E., & Ott, C. D. 2013, *ApJ*, 762, 126
- Ofek, E. O., Sullivan, M., Shaviv, N. J., et al. 2014, *ApJ*, 789, 104
- Ofek, E. O., Cenko, S. B., Shaviv, N. J., et al. 2016, arXiv:1605.02450
- Pastorello, A., Smartt, S. J., Mattila, S., et al. 2007, *Nature*, 447, 829
- Pastorello, A., Cappellaro, E., Inzerra, C., et al. 2013, *ApJ*, 767, 1
- Pejcha, O., & Thompson, T. A. 2015, *ApJ*, 801, 90
- Pejcha, O., & Prieto, J. L. 2015, *ApJ*, 799, 215
- Pier, J. R., Munn, J. A., Hindsley, R. B., et al. 2003, *AJ*, 125, 1559
- Plotkin, R. M., & Clayton, G. C. 2004, *Journal of the American Association of Variable Star Observers (JAAVSO)*, 32, 89
- Quataert, E., & Shiode, J. 2012, *MNRAS*, 423, L92
- Reynolds, T. M., Fraser, M., & Gilmore, G. 2015, *MNRAS*, 453, 2885
- Schaller, G., Schaerer, D., Meynet, G., & Maeder, A. 1992, *A&AS*, 96, 269
- Schlafly, E. F., & Finkbeiner, D. P. 2011, *ApJ*, 737, 103
- Shappee, B. J., Prieto, J. L., Grupe, D., et al. 2014, *ApJ*, 788, 48
- Shiode, J. H., & Quataert, E. 2014, *ApJ*, 780, 96
- Smartt, S. J., Maund, J. R., Hendry, M. A., et al. 2004, *Science*, 303, 499
- Smartt, S. J. 2009, *ARA&A*, 47, 63
- Smartt, S. J. 2015, *PASA*, 32, e016
- Smartt, S. J., Eldridge, J. J., Crockett, R. M., & Maund, J. R. 2009, *MNRAS*, 395, 1409
- Smith, N., & McCray, R. 2007, *ApJL*, 671, L17
- Smith, N., Miller, A., Li, W., et al. 2010, *AJ*, 139, 1451
- Smith, N., Li, W., Silverman, J. M., Ganeshalingam, M., & Filippenko, A. V. 2011, *MNRAS*, 415, 773
- Smith, N. 2014, *ARA&A*, 52, 487
- Smith, N., & Arnett, W. D. 2014, *ApJ*, 785, 82
- Stancliffe, R. J., & Eldridge, J. J. 2009, *MNRAS*, 396, 1699
- Strotjohann, N. L., Ofek, E. O., Gal-Yam, A., et al. 2015, *ApJ*, 811, 117
- Sukhbold, T., & Woosley, S. E. 2014, *ApJ*, 783, 10
- Sukhbold, T., Ertl, T., Woosley, S. E., Brown, J. M., & Janka, H.-T. 2016, *ApJ*, 821, 38
- Szczygiel, D. M., Gerke, J. R., Kochanek, C. S., & Stanek, K. Z. 2012, *ApJ*, 747, 23
- Tinyanont, S., Kasliwal, M. M., Fox, O. D., et al. 2016, arXiv:1601.03440
- Ugliko, M., Janka, H.-T., Marek, A., & Arcones, A. 2012, *ApJ*, 757, 69
- Van Dyk, S. D., Peng, C. Y., King, J. Y., et al. 2000, *PASP*, 112, 1532
- Van Dyk, S. D., Li, W., & Filippenko, A. V. 2003, *PASP*, 115, 1289
- Van Dyk, S. D., Li, W., Cenko, S. B., et al. 2011, *ApJL*, 741, L28
- Walmswell, J. J., & Eldridge, J. J. 2012, *MNRAS*, 419, 2054
- Whitmore, B. C., Allam, S. S., Budavári, T., et al. 2016, *AJ*, 151, 134
- Woosley, S. E., Heger, A., & Weaver, T. A. 2002, *Reviews of Modern Physics*, 74, 1015
- Woosley, S. E., & Heger, A. 2007, *Physics Reports*, 442, 269
- Wongwathanarat, A., Müller, E., & Janka, H.-T. 2015, *AAP*, 577, A48
- Woosley, S. E., & Heger, A. 2015, *ApJ*, 810, 34
- Woosley, S. E. 2016, arXiv:1603.00511
- Zhang, J., Zheng, X., Wang, X., & Rui, L., 2016, *The Astronomer's Telegram*, 9093

Table 1. HST photometry

| Date | Instr. | Exp. (#×sec) | Src. | F435W (mag) | F555W (mag) | F606W (mag) | F658N (mag) | F814W (mag) |
|------------|--------|-----------------|------|----------------|----------------|----------------|----------------|----------------|
| 1994-12-28 | WFPC2 | 2×80 | All | – | – | 23.639±0.099 | – | – |
| 2001-02-24 | WFPC2 | 2×350 | All | – | – | – | – | 22.225±0.041 |
| | | | HSC | – | – | – | – | 22.302±0.083 |
| 2001-03-04 | WFPC2 | 2×350 | All | – | 23.396±0.083 | – | – | – |
| 2001-11-26 | WFPC2 | 160+400 | All | – | – | 23.160±0.038 | – | – |
| 2004-12-31 | ACS | 2×600 | B1 | – | – | – | 22.708±0.081 | – |
| | | | B2 | – | – | – | 24.356±0.315 | – |
| | | | B3 | – | – | – | 24.384±0.323 | – |
| | | | HSC | – | – | – | 22.813±0.075 | – |
| 2004-12-31 | ACS | 2×500 | A1 | 24.149±0.041 | – | – | – | – |
| | | | A2 | 26.034±0.190 | – | – | – | – |
| | | | A3 | 26.011±0.180 | – | – | – | – |
| | | | A4 | 26.250±0.210 | – | – | – | – |
| | | | A5 | 26.189±0.187 | – | – | – | – |
| | | | A6 | 26.727±0.282 | – | – | – | – |
| | | | HSC | 24.097±0.024 | – | – | – | – |
| 2009-12-14 | ACS | 2×260 | C1 | – | 23.899±0.037 | – | – | – |
| | | | C2 | – | 25.015±0.085 | – | – | – |
| | | | C3 | – | 25.392±0.114 | – | – | – |
| | | | C4 | – | 26.259±0.233 | – | – | – |
| | | | C5 | – | 26.889±0.416 | – | – | – |
| | | | C6 | – | 26.254±0.233 | – | – | – |
| | | | C7 | – | 26.119±0.196 | – | – | – |
| | | | HSC | – | 23.768±0.032 | – | – | – |
| 2009-12-14 | ACS | 2×260 | D1 | – | – | – | – | 23.308±0.036 |
| | | | D2 | – | – | – | – | 23.720±0.050 |
| | | | D3 | – | – | – | – | 24.224±0.073 |
| | | | D4 | – | – | – | – | 24.991±0.133 |
| | | | HSC | – | – | – | – | 22.721±0.022 |
| 2013-11-29 | WFC3 | 3×373 | E1 | – | 24.158±0.028 | – | – | – |
| | | | E2 | – | 25.202±0.064 | – | – | – |
| | | | E3 | – | 25.967±0.108 | – | – | – |
| | | | E4 | – | 26.515±0.160 | – | – | – |
| 2013-11-29 | WFC3 | 3×373 | E1 | – | – | – | – | 23.204±0.033 |
| | | | E2 | – | – | – | – | 23.919±0.060 |
| | | | E3 | – | – | – | – | 25.044±0.139 |
| | | | E4 | – | – | – | – | 24.140±0.064 |

The detectors for the WFPC2, ACS and WFC3 instruments were WF3, WFC1 and UVIS2, respectively. The WFPC2/WF3 photometry encompasses “All” of the sources. For WFPC2/WF3 (ACS/WFC1) the HSC AB TotMag (MagAp2) results were converted to Vega magnitudes.

Table 2. LBT R-Band Variability

| Date | MJD | $\Delta L_R (L_\odot)$ |
|------------|----------|------------------------|
| 2008-05-04 | 54590.24 | 184 ± 1236 |
| 2009-01-30 | 54861.34 | −2977 ± 1553 |
| 2009-03-22 | 54912.25 | −2335 ± 1641 |
| 2010-12-13 | 55543.44 | −1771 ± 1570 |
| 2012-01-01 | 55927.44 | −1068 ± 1010 |
| 2012-03-22 | 56008.26 | −221 ± 987 |
| 2012-04-28 | 56045.18 | 3041 ± 1132 |
| 2013-03-16 | 56367.29 | −228 ± 1176 |
| 2013-05-05 | 56417.21 | 330 ± 872 |
| 2014-01-09 | 56666.36 | 549 ± 1273 |
| 2014-04-25 | 56772.20 | −371 ± 734 |
| 2015-01-19 | 57041.32 | −571 ± 1323 |
| 2015-04-20 | 57132.23 | 1604 ± 975 |
| 2016-01-03 | 57390.44 | −80 ± 1064 |
| 2016-02-07 | 57425.29 | 496 ± 1116 |

Table 3. Progenitor Variability

| SN | Time (years) | Burning Phase | RMS (mag) | $\langle \text{Err} \rangle$ (mag) | Var (mag) | Slope (mag/year) | χ^2/dof | Reference |
|-------------|-----------------|-------------------------|--------------|---------------------------------------|--------------|---------------------|---------------------|--------------------------|
| SN 1987a | 91-33 | C Shell | 0.3 | ? | ? | $0.005 \pm ??$ | – | Plotkin & Clayton (2004) |
| SN 1993J | 9.2-8.8 | C Shell | 0.17 | 0.16 | 0.05 | -0.08 ± 0.25 | 53.3/49 | Cohen et al. (1995) |
| SN 2008cn | 12.0-10.8 | C Shell | 0.22 | 0.13 | 0.18 | -0.29 ± 0.10 | 14.2/ 7 | Elias-Rosa et al. (2009) |
| | | | 0.13 | 0.16 | 0 | -0.03 ± 0.12 | 6.1/ 7 | Maund et al. (2015) |
| SN 2011dh | 3.2-0.1 | C \rightarrow O Shell | 0.046 | 0.022 | 0.040 | 0.039 ± 0.006 | 6.7/ 9 | Szczygiel et al. (2012) |
| SN 2013ej | 9.7-8.1 | C shell | 0.0 | 0.03 | 0 | 0.00 ± 0.026 | 0.0/ 0 | Fraser et al. (2014) |
| ASASSN-16fq | 8.1-0.3 | C \rightarrow O Shell | 0.081 | 0.065 | 0.049 | -0.015 ± 0.008 | 16.4/13 | This paper |